Numerical Simulation of Magnetic Resonance Angiographies of an Anatomically Realistic Stenotic Carotid Bifurcation

SYLVIE LORTHOIS,[1] JENN STROUD-ROSSMAN,[2,3] STANLEY BERGER,[2] LIANG-DER JOU,[4] and DAVID SALONER[4]

[1]Institut de Mécanique des Fluides de Toulouse, CNRS UMR 5502, Allées du Professeur Camille Soula, 31400 Toulouse, France; [2]Department of Mechanical Engineering, University of California at Berkeley, Berkeley, CA; [3]Present address: Engineering Department, Harvey Mudd College, Claremont, CA; and [4]Department of Radiology, VA Medical Center, University of California at San Francisco, San Francisco, CA

Abstract—Magnetic Resonance Angiography (MRA) has become a routine imaging modality for the clinical evaluation of obstructive vascular disease. However, complex circulatory flow patterns, which redistribute the Magnetic Resonance (MR) signal in a complicated way, may generate flow artifacts and impair image quality. Numerical simulation of MRAs is a useful tool to study the mechanisms of artifactual signal production. The present study proposes a new approach to perform such simulations, applicable to complex anatomically realistic vascular geometries. Both the Navier-Stokes and the Bloch equations are solved on the same mesh to obtain the distribution of modulus and phase of the magnetization. The simulated angiography is subsequently constructed by a simple geometric procedure mapping the physical plane into the MRA image plane. Steady bidimensional numerical simulations of MRAs of an anatomically realistic severely stenotic carotid artery bifurcation are presented, for both time-of-flight and contrast-enhanced imaging modalities. These simulations are validated by qualitative comparison with flow phantom experiments performed under comparable conditions.

Keywords—Magnetic resonance, Angiography, Bloch equations, Computer simulation, Flow artifacts, Carotid stenoses.

NOMENCLATURE

$\mathcal{A}$	Area
$\boldsymbol{B}(t)$	Time-dependent applied magnetic field
$B_1(t)$	Radio-Frequency pulse
$\mathcal{E}$	Quadrangular element of the physical plane
$(\boldsymbol{i}, \boldsymbol{j}, \boldsymbol{k})$	Laboratory frame of reference
$G_f(t)$	Frequency-encoding gradient
$G_p(t)$	Phase-encoding gradient
$G_{ss}(t)$	Slice selection gradient
$I(X, Y)$	Signal intensity in the image plane
$\mathcal{I}(V)$	Signal intensity in a voxel V
J	Jacobian determinant
$\mathcal{G}_p$	Intensity of the frequency-encoding gradient
$\mathcal{G}_f$	Intensity of the phase-encoding gradient
L	Length of the domain considered
$\boldsymbol{M}$	Magnetization of the spin system
M_0	Longitudinal magnetization before any excitation
M_t	Modulus of the transverse magnetization
$\boldsymbol{n}$	Normal vector of the boundary
$\boldsymbol{r}$	Location of the spin
k_x and k_y	k-Space coordinates
S	MR signal
t	Time
$\mathcal{T}$	Transformation of the physical plane into the image plane
T_1	Longitudinal relaxation time
T_2	Transverse relaxation time
TE	Echo time
T_p	Duration of the phase-encoding
TR	Repetition time
$\boldsymbol{u}$	Spin velocity
U_0	Entry velocity
V	Voxel
x, y	Physical coordinates
X, Y	Image plane coordinates
α	Flip angle
δ	Dirac function
γ	Gyromagnetic ratio
φ	Phase of the transverse magnetization
φ_0	Reference phase for stationnary spins
$\tilde{\varphi}$	Total motion-dependent phase
$\tilde{\varphi_f}$	Motion-dependent phase accumulated through the frequency-encoding gradient
$\tilde{\varphi_p}$	Motion-dependent phase accumulated through the phase-encoding gradient
τ	Duration of the readout-range

Address correspondence to Sylvie Lorthois, Institut de Mécanique des Fluides de Toulouse, Groupe d'Etude sur les Milieux Poreux, Allées du Professeur Camille Soula, 31400 Toulouse Cedex, France. Electronic mail: lorthois@imft.fr

INTRODUCTION

There is an increasing acceptance of Magnetic Resonance Angiography (MRA) as a modality for the clinical evaluation of obstructive vascular disease.[13] However, complex flow patterns, such as convective accelerations, recirculation areas, vortical structures, and pulsatile flows, may produce flow artifacts like intravoxel phase dispersion (IVPD) and misregistration effects.[8,9,17,27] These effects are encountered both at sites of severe stenoses, even if situated in a straight vessel, and at sites of curves or vessel branching, which are preferential areas for the development of atherosclerotic disease. They result in a complex redistribution of the MR signal which creates image artifacts that are difficult to interpret in an intuitive manner. For example, flow-induced signal loss is often observed both upstream and downstream of stenoses, thereby making the differentiation between severe stenoses and occlusions difficult or even impossible.[19,20,26] Thus, such artifacts can lead to misinterpretations of imaging studies and inappropriate patient treatment.

For about a decade, numerical simulations of MRA have emerged as one of the essential tools for understanding the mechanisms of artifactual signal production and their implication for *in vivo* imaging. Simple model geometries (such as curved tubes [8,27] and axisymmetric plug flow[7,19] or streamlined stenoses[20]) and more complex idealized geometries (such as a bypass graft end-to-side anastomosis[21] or a bidimensional healthy carotid bifurcation[27]) have been studied by means of a Lagrangian approach. In this approach, spin trajectories are obtained by a computational fluid dynamics (CFD) simulation. The temporal evolution of magnetization along spin trajectories is subsequently calculated by integrating the Bloch equations following each trajectory.

This is an intuitive approach, as analytic solutions of the Bloch equations along spin trajectories are known. In most cases (i.e. most geometries and imaging conditions, from time of flight (TOF) MR angiography to phase contrast (PC) velocity measurements), simulated MR images compare favorably with MR experiments performed on flow phantoms of identical geometry in equivalent conditions.

However, in flow configurations exhibiting high velocity gradients near the vessel wall (for example in curved tubes), important discrepancies appear due to the difficulty of tracking spin trajectories near the wall.[8] Even in regions not containing complex velocity fields, high spatial resolutions are required near the wall to adequately resolve subtle changes in geometry.[25] In addition, in the Lagrangian approach, many spin trajectories must be computed in order to correctly account for intravoxel phase dispersion and misregistration effects, which requires extensive computation time. The time-consuming nature of these calculations renders prohibitive the extension of Lagrangian-based numerical calculations to complex anatomically realistic geometries.

In such geometries, the Eulerian approach developed by Jou *et al*.[8,9,17] seems more convenient. Briefly, the velocity field, i.e., the three components of the velocity vector at each point of a mesh, is obtained by a CFD simulation. This velocity field is used to solve the Bloch equations in Eulerian formulation,[6] which describe the inflow and outflow of magnetization at each point of the domain as a function of magnetization at neighboring points. These equations are solved numerically on the same mesh used by the CFD simulation, without requiring spin trajectories to be tracked. Misregistration effects arise from fluid motion between the time of phase-encoding (at that time, the phase generated by the phase-encoding gradient at each mesh node is proportional to the y-position of the node) and the time of readout. Thus, in order to account for misregistration effects, the initial mesh is transformed to the corresponding mesh of the image plane by determining the transformed y-position of each node from its phase at the time of readout. The apparent proton density in the reconstructed image plane is given by the jacobian of this transformation, and accounts for the component of the intravoxel phase dispersion (IVPD) effect generated by the phase-encoding gradient. Signal intensity in the image plane is subsequently calculated, assuming the magnetization modulus and phase within a voxel to be bilinear, by searching all the quadrangles of the initial mesh that map to this voxel. By contrast to the Lagrangian approach, the Eulerian approach has been successfully used to simulate MRAs in curved tubes.[8,17] In addition, the computation time reduction allowed the simulation of MRAs of a bidimensional healthy carotid bifurcation with pulsatile flow.[9]

In parallel with these advances in MRA simulation, the development of efficient numerical methods and new computer capabilities has made possible the calculation of blood flow in anatomically realistic geometries.[2,3,11,12,14,22,23] In particular, such calculations have shown that minor details of the vascular geometry (surface irregularities, curvature, *etc*.) can affect the flow significantly, even relatively far away from their location.

Thus, performing numerical simulations of MRAs in complex anatomically realistic geometries seems attainable in the near future. In this paper, the case of a severely stenotic carotid artery bifurcation with realistic shape will be presented. However, because of the complexity of the geometry involved, only the steady flow through a two-dimensional model of this bifurcation will be considered. This simplified test case will be studied following the Eulerian approach described above,[8,9,17] revisited in a signal processing perspective, and with further improvements of the phase-averaging procedure.

Both time of flight and contrast-enhanced (CE) MRAs will be simulated. The TOF technique relies on inflowing blood to transport full magnetization into the image

volume resulting in signal enhancement and high vessel to background contrast and on velocity-compensated gradient echo sequences to retain all transverse magnetization. Unfortunately, this technique requires long repetition times in order to avoid blood signal saturation, which makes it difficult to reduce flow artifacts. To achieve good vessel contrast with a short repetition time, a contrast agent, such as gadolinium, can be used to reduce the longitudinal relaxation time T_1 of blood. In order to achieve the very short echo times needed, no velocity compensation is used in the gradient echo sequences. Vessel contrast, in this so-called contrast-enhanced MRA technique (CE-MRA), is then due to T_1 effects instead of inflow effects as in TOF. Qualitative comparisons of the simulated MRAs with MR phantom experiments performed in comparable conditions will be presented.

METHODS

Severely Stenotic Carotid Artery Bifurcation Model

Surgical treatment of carotid artery disease involves opening the artery and removing the plaque lining the vessel wall, a procedure known as an endarterectomy. One of the plaques was resected *en bloc* in one intact piece at the San Francisco VA Medical Center [specimen provided by Dr. Joseph Rapp, Associate Professor of Vascular Surgery, UCSF/VA Medical Center, to the author (DS)]. This specimen was imaged using Magnetic Resonance Imaging at high resolution (200 μm^3) and the lumenal contour was obtained by image postprocessing.

Because of the complexity of the geometry involved, only a two-dimensional model based on one coronal plane of the three-dimensional contour has been considered (Fig. 1). This simplification is consistent with the numerical analysis of flow through the same two-dimensional stenotic bifurcation performed by Stroud *et al.*,[23] which aimed to supplement MR and other *in vivo* diagnostic techniques to provide an accurate picture of the clinical status of particular vessels.

In addition, a phantom, i.e., a three-dimensional true-to-scale physical model with nearly rigid wall, was constructed in silicone (silastic) rubber (Fig. 2.) in order to make qualitative comparisons between MR simulations and experiments performed in equivalent conditions.[26]

Simulation of Magnetic Resonance Angiographies

Simulation of MRAs by means of the Eulerian approach requires the calculation of the velocity field in the geometry described above. This calculation has been previously reported.[23] Briefly, the incompressible, steady Navier-Stokes equations for a Newtonian fluid are solved using a finite-volume CFD software package (From CFD Research Corporation, Hunstville, AL) on the grid displayed on Fig. 1. The boundary conditions are uniform

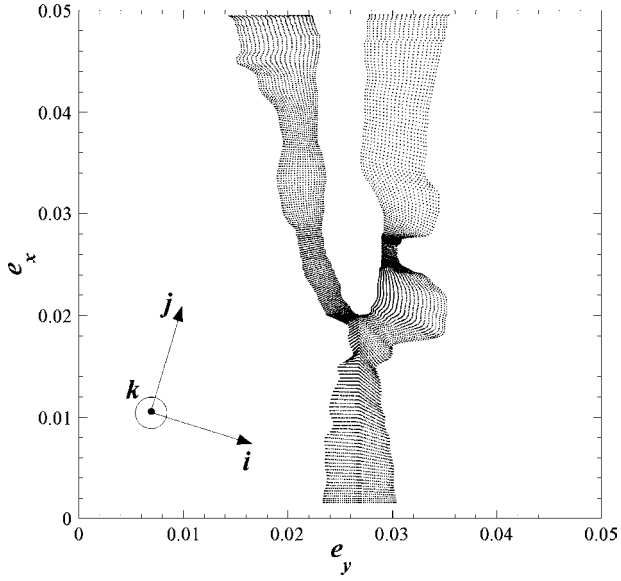

FIGURE 1. *Model Geometry*: Two-dimensional structured grid (9040 vertices, 8775 quadrangular elements) used in CFD computations (scale in meters). (i, j, k) is the laboratory frame of reference and k defines the longitudinal direction. When phase encoding is aligned with the main-flow direction, then $e_x = i$ and $e_y = j$; when phase encoding is perpendicular to the main-flow direction, then $e_x = j$ and $e_y = i$.

FIGURE 2. *Model Geometry*: Phantom used in MR experiments.

inlet flow ("plug" flow), fixed pressure (equivalent to flow through) at the outlet, and no-slip at wall. Note that the resulting flow contains large recirculation areas, large spatial variations in wall shear, and high velocity gradients near the vessel wall (see ref. 23).

Transport of Magnetization

The Bloch equations in Eulerian formulation[6] are the following:

$$\frac{\partial \boldsymbol{M}}{\partial t} + (\boldsymbol{u}\cdot\nabla)\,\boldsymbol{M} = \gamma\,\boldsymbol{M}\times\boldsymbol{B}(t) - \frac{M_x\boldsymbol{i} + M_y\boldsymbol{j}}{T_2} + \frac{M_0 - M_z}{T_1}\boldsymbol{k}, \quad (1)$$

where bold symbols are used to denote vectors and $(\boldsymbol{i}, \boldsymbol{j}, \boldsymbol{k})$ is the laboratory frame of reference (see Fig. 1. for the definition of axes). In these equations, $\boldsymbol{M}$ is the magnetization of a fluid element, originating from the presence of water protons, and M_0 is its longitudinal magnetization before any excitation. The fluid velocity $\boldsymbol{u}$ is calculated as described above. The gyromagnetic ration is γ, T_1, and T_2 are the longitudinal and transverse relaxation times, and $\boldsymbol{B}(t)$ is the time-dependent applied magnetic field:

$$\boldsymbol{B}(t) = (B_0 + \boldsymbol{G}(t)\cdot\boldsymbol{r})\,\boldsymbol{k} + B_1(t)(\cos(\gamma B_0 t)\boldsymbol{i} - \sin(\gamma B_0 t)\,\boldsymbol{j}), \quad (2)$$

with

$$\boldsymbol{G}(t) = G_f(t)\boldsymbol{i} + G_p(t)\,\boldsymbol{j} + G_{ss}(t)\boldsymbol{k}. \quad (3)$$

In the above expressions, $\boldsymbol{r}$ is spin position vector, B_0 is the static magnetic field, $B_1(t)$ is the radio-frequency (RF) pulse[10] used to rotate the longitudinal magnetization into the transverse plane, i.e., $(\boldsymbol{i}, \boldsymbol{j})$ plane, and $G_f(t)$, $G_p(t)$, and $G_{ss}(t)$, respectively, denote the frequency encoding, phase encoding, and slice selection gradients. The timing diagram for this pulse sequence is schematized on Fig. 3. The values of the parameters used in both TOF and CE simulations are presented in Table 1. For CE-MRA, injection of the contrast agent, such as gadolinium, is modeled by reducing the blood longitudinal relaxation time T_1 uniformly in space and time, which is an additional simplification.[24]

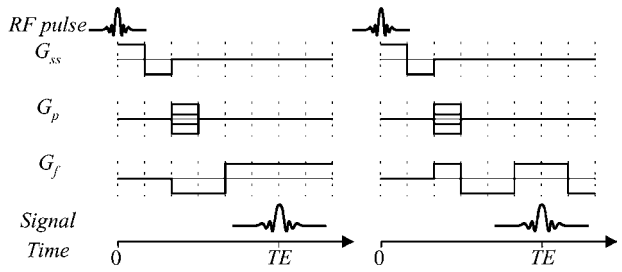

FIGURE 3. Schematic timing diagram of a single repetition cycle of a gradient echo sequence. *Left*: Velocity uncompensated gradient; *Right*: Velocity compensated gradient. Note that cycles are separated by the repetition time TR. TE is the echo time.

TABLE 1. Values of the parameters used for the simulation of TOF and CE MRAs. VC: Velocity compensated gradients; VU: Velocity uncompensated gradients.

	T_1 (ms)	TR (ms)	TE (ms)	α (degrees)	Sequence
TOF	1000	30	7	20	VC
CE	200	7	3	20	VU

The set of partial differential equations [Eq. 1] can be rewritten using $M_x = M_t\cos\varphi$ and $M_y = M_t\sin\varphi$, where M_t and φ are the modulus and phase of transverse magnetization. In addition, in the following, this set will be simplified considering the different steps of the imaging sequence.

a. Excitation range: Since the duration of the excitation pulse is very short compared with the relaxation times T_1 and T_2 (see Table 2), relaxation effects can be neglected during the excitation pulse. The spin transit time (evaluated by L/U_0, where L is the length of the domain considered and U_0 is the entry velocity) is large compared to the duration of the RF pulse (see Table 2). Thus, convective transport of magnetization by blood flow [term $(\boldsymbol{u}\cdot\nabla)\,\boldsymbol{M}$ in Eq. (1)] can also be neglected.

In addition, the exact temporal dependence of the RF pulse is designed as a function of the slice selection gradient G_{ss} in order to produce a block rotation of the spins contained in the selected slice.[28] As the studied domain is two-dimensional, the selected slice corresponds to the whole domain. Thus, the coupled effect of the RF pulse and of the slice-selection gradient is to flip the magnetization vector around the direction of the RF pulse (contained in the transverse plane) and to produce a simultaneous rephasing of the spins:

$$M_z^+ = M_z^-\cos\alpha,\ \ M_t^+ = M_z^-\sin\alpha,\ \ \varphi^+ = 0, \quad (4)$$

where $^+$ and $^-$ respectively denote the instants just after and just before excitation, and α is the flip angle.

b. Relaxation range: During the relaxation phase, $\boldsymbol{B}(t)$ is directed along $\boldsymbol{k}$. Thus, the Bloch equations [Eq. (1)] lead to

$$\frac{\partial M_z}{\partial t} + \boldsymbol{u}\cdot\nabla M_z = \frac{M_0 - M_z}{T_1}, \quad (5)$$

TABLE 2. Order of magnitude of the characteristic times for relaxation (T_1 and T_2), transit (L/U_0), excitation range (T_{exc}), relaxation range (TE), and readout (τ) (in ms).

T_1	T_2	L/U_0	T_{exc}	TE	τ
200–1000	50	150–300	3	3–7	3–7

$$\frac{\partial M_t}{\partial t} + \boldsymbol{u} \cdot \boldsymbol{\nabla} M_t = \frac{-M_t}{T_2}, \tag{6}$$

and

$$\frac{\partial \varphi}{\partial t} + \boldsymbol{u} \cdot \boldsymbol{\nabla} \varphi = -\gamma \left(B_0 + \boldsymbol{G}(t) \cdot \boldsymbol{r} \right). \tag{7}$$

In addition, in the sequences considered, the echo time (TE) is very short compared to the relaxation time T_2 and to the spin transit time (see Table 2). Thus, from Eqs. (4) and (6)

$$M_t\,(\mathrm{TE}) \simeq M_t^+ = M_z^+ \tan\alpha, \tag{8}$$

which means that image appearance is unaffected by transverse relaxation.

Let us introduce φ_0, the reference phase for stationary spins [i.e., the solution of Eq. (7) when $\boldsymbol{u} \equiv 0$)]:

$$\varphi_0 = -\gamma \left(B_0 t + \boldsymbol{r} \cdot \int_0^t \boldsymbol{G}(\xi)\, d\xi \right). \tag{9}$$

We introduce $\tilde{\varphi_f}$ and $\tilde{\varphi_p}$, the motion-dependent phases accumulated through the frequency-encoding and phase-encoding gradients, which respectively satisfy:

$$\frac{\partial \tilde{\varphi_f}}{\partial t} + \boldsymbol{u} \cdot \boldsymbol{\nabla} \tilde{\varphi_f} = \gamma\, \boldsymbol{u} \cdot \boldsymbol{i} \int_0^t G_f(\xi)\, d\xi, \tag{10}$$

and

$$\frac{\partial \tilde{\varphi_p}}{\partial t} + \boldsymbol{u} \cdot \boldsymbol{\nabla} \tilde{\varphi_p} = \gamma\, \boldsymbol{u} \cdot \boldsymbol{j} \int_0^t G_p(\xi)\, d\xi, \tag{11}$$

so that, from Eqs. (7) and (9)

$$\varphi = \varphi_0 + \tilde{\varphi_f} + \tilde{\varphi_p}. \tag{12}$$

Equations (5), (10), and (11) are numerically solved by a marching predictor–corrector method, on the same grid used for the CFD computation, with the following entry conditions:

– $M_z = M_0$ (incoming blood has not been subjected to any RF excitation and is thus unsaturated),
– $\boldsymbol{n} \cdot \boldsymbol{\nabla} \tilde{\varphi_f} = 0$ and $\boldsymbol{n} \cdot \boldsymbol{\nabla} \tilde{\varphi_p} = 0$, where $\boldsymbol{n}$ is the normal vector of the simulation domain boundary.

The initial conditions for each repetition cycle, whose duration is the repetition time TR, are given by Eq. (4). Note that the resulting initial conditions for $\tilde{\varphi_f}$ and $\tilde{\varphi_p}$ ($\tilde{\varphi_f}^+ = 0$ and $\tilde{\varphi_p}^+ = 0$) are independent of the number of anterior repetition cycles performed. Thus, $\tilde{\varphi_f}$ and $\tilde{\varphi_p}$ temporal evolutions are the same for each repetition cycle. On the contrary, the initial condition for M_z at a given repetition cycle depends on its value at the end of the previous repetition cycle. Equation (5) is therefore solved until the distribution of longitudinal magnetization does not change with additional RF excitation, i.e., the dynamic equilibrium is reached.

Signal Expression

In the following, $\mathcal{G}_p$ and $\mathcal{G}_f$ denote the intensities of the phase and frequency encoding gradients when not set to zero, and T_p denotes the duration of the phase encoding. The MR signal $S(t, \mathcal{G}_p)$ is given by

$$S(t, \mathcal{G}_p) = \int_x \int_y M_t(x, y, t) e^{i(\varphi_0(x,y,t) + \tilde{\varphi_f}(x,y,t) + \tilde{\varphi_p}(x,y,t))}\, dx\, dy. \tag{13}$$

During the readout range (of duration τ), i.e for $\mathrm{TE} - \tau/2 \le t \le \mathrm{TE} + \tau/2$, and according to the timing diagram sketched on Fig. 3, Eq. (9) gives:

$$\varphi_0(x, y, t) = -\gamma \left(B_0 t + y \mathcal{G}_\mathrm{p} T_\mathrm{p} + x \int_0^{\mathrm{TE}} G_f(t)\, dt + (t - \mathrm{TE}) x\, \mathcal{G}_f \right). \tag{14}$$

From sequence design (see Fig. 3), $x \int_0^{\mathrm{TE}} G_f(t)\, dt$ equals zero. Thus, using TE as a new time reference and using Eq. (8), we have

$$S(t, \mathcal{G}_p) = \int_x \int_y M_z^+(x, y) \times \tan\alpha\, e^{i(-\gamma\left(B_0(t+\mathrm{TE}) + y\mathcal{G}_p T_p + x\mathcal{G}_f t\right) + \tilde{\varphi_f}(x,y,t) + \tilde{\varphi_p}(x,y,t))}\, dx\, dy. \tag{15}$$

This signal is a high frequency signal because the transverse magnetization vector precesses at the Larmor frequency, as observed in the laboratory frame. In practice, $S(t)$ is moved to a low frequency band using a *signal demodulation* method[10]:

$$S(t, \mathcal{G}_\mathrm{p}) = \int_x \int_y M_z^+(x, y) \times \tan\alpha\, e^{i(-\gamma\left(y\mathcal{G}_\mathrm{p} T_\mathrm{p} + x\mathcal{G}_\mathrm{f} t\right) + \tilde{\varphi_\mathrm{f}}(x,y,t) + \tilde{\varphi_\mathrm{p}}(x,y,t))}\, dx\, dy. \tag{16}$$

Interestingly, due to the signal demodulation, this expression is equivalent to the expression that would be obtained by resolution of the Eulerian Bloch equations written in the rotating frame but with $\boldsymbol{u}$ kept in the laboratory frame.

Spatial Decoding

Let us introduce the k-space coordinates:

$$k_x = -\gamma \mathcal{G}_f t,\ k_y = -\gamma \mathcal{G}_p T_p. \tag{17}$$

Note that

– for steady flow, Eq. (11) implies that $\tilde{\varphi_p}$ is proportionnal to $\mathcal{G}_p$, and thus to k_y (note that this is still true for periodic flows if the beginning of each repetition cycle

corresponds to the same instant of the flow period). It can then be expressed as

$$\tilde{\varphi_p}(x, y, t) = k_y \tilde{y}(x, y, t), \tag{18}$$

– since the duration of the readout range is very short compared to the spin transit time (Table 2) and to the characteristic times for precession in Eq. (10) and (11) (see Appendix A), $\tilde{y}$, and $\tilde{\varphi_f}$ may be considered as independent of t during the readout range, and equal to their values at TE (i.e. origin of the new time frame). $\tilde{y}$ and $\tilde{\varphi_f}$ are therefore independent of k_x.
– in addition, from Eq. (10), $\tilde{\varphi_f}$ is independent of $\mathcal{G}_p$ and thus of k_y,

Equation (16) thus becomes in k-space:

$$S(k_x, k_y) = \int_x \int_y \mathcal{M}(x, y) e^{i(k_x x + k_y (y + \tilde{y}(x,y))} \, dx \, dy, \tag{19}$$

where $\mathcal{M}(x, y) = M_z^+(x, y) \tan \alpha \, e^{i\tilde{\varphi_f}(x,y)}$. The signal intensity in the image plane, described by its coordinates X and Y, is given by the inverse Fourier transform of $S(k_x, k_y)$:

$$I(X, Y) = \frac{1}{(2\pi)^2} \int_{k_x} \int_{k_y} S(k_x, k_y) \, e^{-i(k_x X + k_y Y)} \, dk_x \, dk_y. \tag{20}$$

By inverting the integration order,[18] we obtain:

$$I(X, Y) = \frac{1}{(2\pi)^2} \int_x \int_y \mathcal{M}(x, y) \, dx \, dy \int_{k_x} e^{ik_x(x - X)} \, dk_x \times \int_{k_y} e^{ik_y(y + \tilde{y}(x,y) - Y)} \, dk_y \tag{21}$$

Finally, as $\int_{k_x} e^{ik_x x} \, dk_x = \delta(x)$, where δ is the Dirac function, we deduce:

$$I(X, Y) = \frac{1}{(2\pi)^2} \int_x \int_y \mathcal{M}(x, y) \delta(x - X) \times \delta(y + \tilde{y}(x, y) - Y) \, dx \, dy \tag{22}$$

Let us introduce transformation $\mathcal{T}$: $(x, y) \mapsto (\hat{x}, \hat{y})$ of space:

$$\hat{x} = x, \;\; \hat{y} = y + \tilde{y}(x, y). \tag{23}$$

Let first assume that transformation $\mathcal{T}$ is a bijection, and denote by $\mathcal{T}^{-1}$ the inverse transformation. Using $\hat{x}$ and $\hat{y}$ as new variables, Eq. (22) rewrites:

$$I(X, Y) = \frac{1}{(2\pi)^2} \int_{\hat{x}} \int_{\hat{y}} \mathcal{M} \circ \mathcal{T}^{-1}(\hat{x}, \hat{y}) \delta(\hat{x} - X) \times \delta(\hat{y} - Y) \, J_{\mathcal{T}^{-1}}(\hat{x}, \hat{y}) \, d\hat{x} \, d\hat{y}, \tag{24}$$

where $J_{\mathcal{T}^{-1}}$ is the Jacobian of transformation $\mathcal{T}^{-1}$. Thus:

$$I(X, Y) = \frac{1}{(2\pi)^2} \mathcal{M} \circ \mathcal{T}^{-1}(X, Y) J_{\mathcal{T}^{-1}}(X, Y), \tag{25}$$

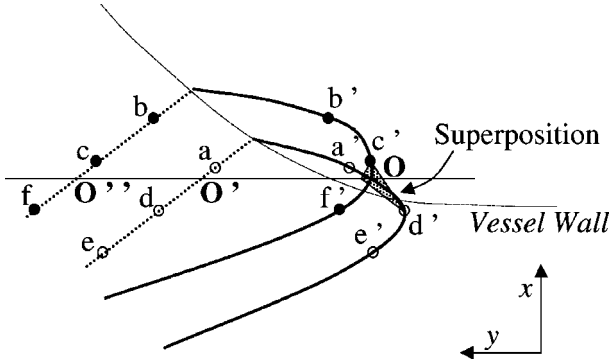

FIGURE 4. Transformation $\mathcal{T}$ of the physical plane into the image plane. The schematized situation corresponds to a flow from right to left with a peak velocity profile close to the vessel wall, as observed in the vicinity of the bifurcation apex. Continuous lines (a', d', e') and (b',c',f') are the images of dotted lines (a, d, e) and (b,c,f). They intersect in O which has therefore two antecedents (O' and O") by $\mathcal{T}$. In addition, images of the distinct quadrangles (a,b,c,d) and (c,d,e,f) of the physical plane are the superposed quadrangles (a',b',c',d') and (c',d',e',f') of the image plane.

Finally, the signal intensity $\mathcal{I}$ in a voxel V is the sum of $I(X, Y)$ over the whole voxel:

$$\mathcal{I}(V) = \frac{1}{(2\pi)^2} \int \int_V \mathcal{M} \circ \mathcal{T}^{-1}(X, Y) J_{\mathcal{T}^{-1}}(X, Y) \, dX \, dY, \tag{26}$$

which simplifies to

$$\mathcal{I}(V) = \frac{1}{(2\pi)^2} \int \int_{\mathcal{T}^{-1}(V)} \mathcal{M}(x, y) \, dx \, dy, \tag{27}$$

where $\mathcal{T}^{-1}(V)$ is the image of voxel V by transformation $\mathcal{T}^{-1}$.

However, transformation $\mathcal{T}$ is not a bijection, because some points in the transformed plane may have more than one antecedent (see Fig. 4). Nevertheless, Eq. (27) still holds (see Appendix B for a one-dimensional demonstration), which calls for several comments.

First, as indicated by Eq. (24), it appears that the image plane coordinates X and Y *do not* correspond to x and y, physical coordinates of the carotid bifurcation, but to $\hat{x}$ and $\hat{y}$. In other words, the misregistration components are $(\hat{x} - x, \hat{y} - y)$, i.e., $(0, \tilde{y})$. Second, the local signal intensity in the image plane equals the corresponding local intensity in the physical plane ($\mathcal{M} \circ \mathcal{T}^{-1}$) multiplied by the Jacobian of transformation $\mathcal{T}^{-1}$ [see Eq. (25)]. This jacobian represents the apparent proton density in the image plane. Third, from Eq. (27), the signal intensity in a voxel equals the sum of the local magnetization $\mathcal{M}$ in the physical plane over the physical area matching the image plane voxel after misregistration.

Image Construction

The simulated MRA is constructed by evaluating the contribution to the voxel V of each quadrangular element

$\mathcal{E}$ of the grid used for the CFD calculation:

$$\mathcal{I}(V, \mathcal{E}) = I_{\mathcal{E}} \frac{\mathcal{A}(\mathcal{T}(\mathcal{E}) \cap V)}{\mathcal{A}(\mathcal{T}(\mathcal{E}))}, \tag{28}$$

where $\mathcal{A}(\mathcal{T}(\mathcal{E}))$ and $\mathcal{A}(\mathcal{T}(\mathcal{E}) \cap V)$ respectively denote the areas of the image plane element $\mathcal{T}(\mathcal{E})$ and of its intersection with V and $I_{\mathcal{E}}$ denotes the total intensity contribution of $\mathcal{E}$ evaluated by

$$I_{\mathcal{E}} = \frac{1}{4} \left(\sum_{j=1}^{4} \mathcal{M}(x_j, y_j) \right) \mathcal{A}(\mathcal{E}), \tag{29}$$

where (x_j, y_j) are the four edges of $\mathcal{E}$ and $\mathcal{A}(\mathcal{E})$ is its area.

Thus, image construction requires the calculation of the following areas: $\mathcal{A}(\mathcal{E})$, $\mathcal{A}(\mathcal{T}(\mathcal{E}))$, and $\mathcal{A}(\mathcal{T}(\mathcal{E}) \cap V)$, as summarized in Appendix C. Note that, due to misregistration, $\mathcal{T}(\mathcal{E})$ is not necessarily a simple quadrangle but may be self-intersecting. Area calculations are checked by summing the intersections of $\mathcal{T}(\mathcal{E})$ with every voxel of the image plane, and comparing with $\mathcal{A}(\mathcal{T}(\mathcal{E}))$.

Finally, the (complex) signal intensity $\mathcal{I}$ in the voxel V is the sum of the contributions of each quadrangular element whose image by transformation $\mathcal{T}$ has a non-null intersection with V. The simulated MRA is constructed by mapping the voxel intensity modulus to 255 grey levels (GL):

$$\mathrm{GL}(V) = \max \left(\mathrm{Trunc} \left(255 \frac{|\mathcal{I}(\mathrm{V})|}{|\mathcal{I}(\mathrm{V_{ref}})|} \right), 255 \right), \tag{30}$$

where V_{ref} is an entry reference voxel.

Flow Phantoms Experiments

The flow phantom experiments were performed on a commercial scanner (1.5-T Siemens Magnetom, Siemens Medical Systems, Erlangen, Germany) using 3D time of flight or contrast-enhanced MRA gradient echo sequences. The head coil was used as the receiver coil. A steady water flow was used. The mean velocity in the common carotid artery, evaluated by inversion bolus tagging before image collection, was $0.14\,\mathrm{ms}^{-1}$.

For TOF sequences, parameters were as follows: TR/TE/flip angle = 30 ms/6 ms/20° with velocity compensation along slice-selection and frequency-encoding directions. In-plane resolution was 0.7 mm × 0.7 mm with slice thickness of 1 mm.

For CE sequences, a 60 ml bolus of Gd-DTPA (gadalonium) at a concentration of 1:60 was injected over 20 s. A timing run was performed to determine transit time between injection and arrival in the flow phantom. Imaging parameters were as follows TR/TE/flip angle = 6 ms/2.2 ms/25°. In-plane resolution was 0.5 mm × 0.86 mm with slice thickness of 1.6 mm.

RESULTS AND DISCUSSION

The complex flow pattern in the severely stenotic carotid bifurcation has been described in Stroud *et al.*[23] As already mentioned, the flow contains large recirculation zones and strong jet areas, resulting in high spatial variations in shear stress. In particular, there is a large recirculation region filling the carotid sinus upstream of the point of maximum stenosis, the spatial extent of which is independent of the Reynolds number. A second elongated recirculation zone, downstream of the stenosis throat, enlarges with increasing Reynolds number. The strongest jet is observed in the entry region of the common carotid artery, where the maximum velocity is almost four times the entry velocity, independently of the Reynolds number.

Transport of Magnetization

Isovalues of the TOF equilibrium longitudinal magnetization M_z are plotted on Fig. 5., for two values of the inlet Reynolds number (based on the inlet diameter and mean velocity and for a kinematic viscosity of $3.4 \times 10^{-6}\,\mathrm{m^2\,s^{-1}}$).

Equilibrium magnetization is maximal at the inlet of the common carotid artery, due to entry of "fresh" blood, not subjected to any RF excitation (i.e. $M_z = M_0$). Using the Lagrangian approach, it can be shown that, for a given set of imaging parameters T_1 and TR, equilibrium magnetization only depends on the number of RF pulses experienced by the fluid during its motion from the inlet. In other words, equilibrium magnetization only depends on the transit time, as displayed in Fig. 6. Thus, isovalues of the equilibrium magnetization and isovalues of transit time from the inlet are superimposed. When the inlet Reynolds number

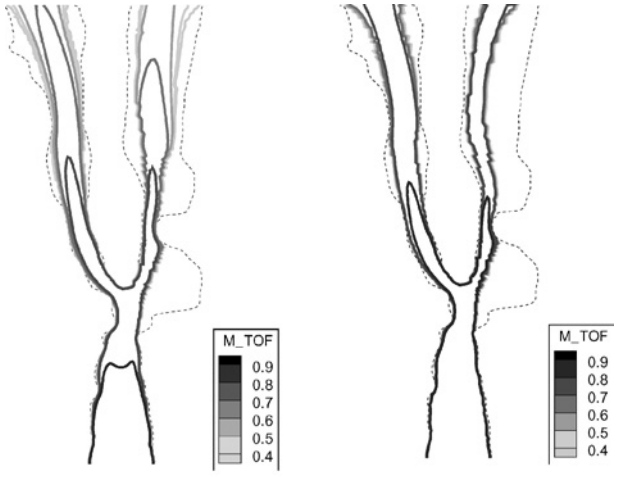

FIGURE 5. Isovalues of the TOF equilibrium magnetization M_z normalized by M_0, the longitudinal magnetization before any excitation. Reynolds number at the inlet of the common carotid artery is 300 (*left*) and 600 (*right*). Parameters used are listed in Table 1. The dashed line outlines the vessel wall.

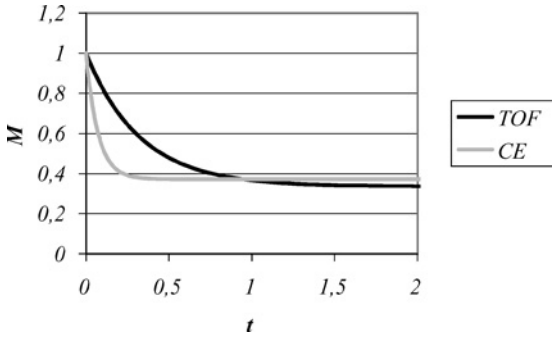

FIGURE 6. Equilibrium magnetization normalized by M_0 as a function of transit time (s), for TOF and CE sequences. Parameters used are listed in Table 1.

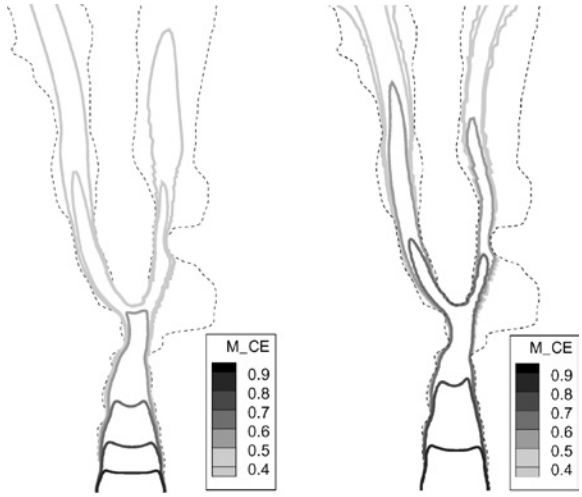

FIGURE 7. Isovalues of the CE equilibrium magnetization M_z normalized by M_0, the longitudinal magnetization before any excitation. Reynolds number at the inlet of the common carotid artery is 300 (*left*) and 600 (*right*). Parameters used are listed in Table 1. The dashed line outlines the vessel wall.

increases from 300 to 600, "fresh" blood is convected faster, longitudinal magnetization decreases more slowly following the flow direction and the inflow effect is strengthened. Concurrently, the elongated recirculation zone located downstream of the stenosis throat enlarges, deflecting the "fresh" blood region toward the internal carotid artery divider wall.

Because the flow field displays recirculation areas and because the geometry considered is bidimensional, the fluid contained in these recirculations areas is "trapped," i.e. there is no mechanism to bring unsaturated spins from the main flow into these areas. Thus, in the recirculation areas, blood is fully saturated and its equilibrium magnetization corresponds to the magnetization of stationary spins M_∞ calculated with an infinite transit time:

$$M_\infty = \frac{1 - e^{-\mathrm{TR}/T_1}}{1 - \cos(\alpha)\mathrm{e}^{-\mathrm{TR}/\mathrm{T}_1}} \tag{31}$$

Note that the spatial extent of these fully saturated zones is overestimated because, in the equivalent three-dimensional stenotic flow field, out of plane velocity components may be significant to mix fluid from the main flow and fluid from the recirculation areas (see the experimental work of Bale-Glickman *et al.*[1])

Isovalues of the CE equilibrium longitudinal magnetization M_z are plotted on Fig. 7. As before, when the inlet Reynolds number increases, inflow effect is more pronounced. However, it is markedly reduced compared to the TOF simulation.

Figure 8 simultaneously displays isovalues of the image plane coordinate $\hat{y}$ (continuous lines) and of the motion-dependent phase accumulated through the frequency-encoding gradient $\tilde{\varphi_f}$ (color map) in both TOF and CE conditions, when phase encoding is perpendicular to the main flow direction. Misregistration is demonstrated by the distortion of the $\hat{y}$ isovalues, which would be vertical lines for stationary spins (for stationary spins, $\tilde{y} = 0$ and $\hat{y} = y$). In both TOF and CE conditions, misregistration is maximal at the edge of the bifurcation and in the main recirculation area situated upstream of the stenosis, where velocities perpendicular to the main flow direction are observed. Because the time between phase encoding and readout is smaller in the CE sequence, misregistration is smaller in CE conditions. On the contrary, as the CE frequency-encoding gradient is not velocity compensated, the amplitude of the $\tilde{\varphi}_\mathrm{f}$ variation is larger even if the CE sequence duration is shorter. Positive values of $\tilde{\varphi_f}$ are observed when the velocity component in the main flow direction is positive, whereas negative values are observed when the velocity component in the main flow direction is negative. Strong phase gradients are noticed at the surrounding of the flow jet in the internal carotid artery (including along the walls at the stenosis throat) and along the walls in the external carotid artery, where velocity gradients in the main flow direction are elevated. These phase gradients will produce significant IVPD after image construction. In TOF conditions, due to velocity compensation, positive values of $\tilde{\varphi}_\mathrm{f}$ are observed when the acceleration in the main flow direction is positive (stenosis throat, end of the common carotid artery), whereas negative values are observed when the acceleration in the main flow direction is negative (downstream of the stenosis throat, bifurcation apex).

Figure 9 simultaneously displays isovalues of the image plane coordinate $\hat{y}$ (continuous lines) and of the motion-dependent phase accumulated through the frequency-encoding gradient $\tilde{\varphi_f}$ (color map) in both TOF and CE conditions, when frequency encoding is perpendicular to the main flow direction. Misregistration is demonstrated by the distortion of the $\hat{y}$ isovalues, which would be horizontal lines for stationary spins. In both TOF and CE conditions, misregistration is maximal at the end of the common carotid artery and at the stenosis throat, where elevated velocities in the flow direction are observed. Areas of retrograde

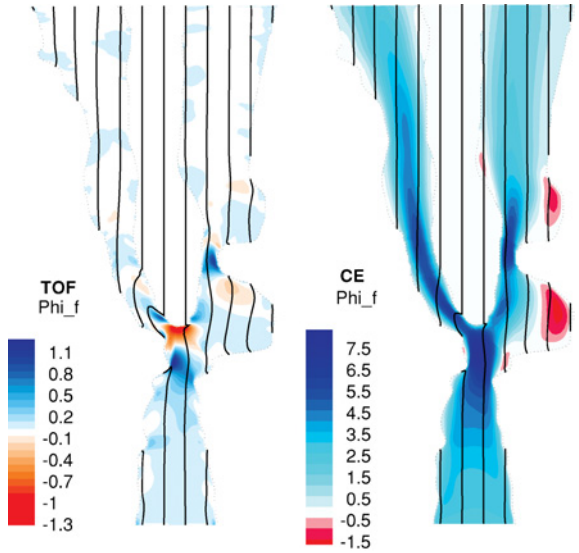

FIGURE 8. Isovalues of the phase $\tilde{\varphi_f}$ (color map) and of the image plane coordinate $\hat{y}$ (continuous lines) obtained with TOF parameters (left) and CE parameters (right). Phase encoding is perpendicular to the main flow direction. Reynolds number at the inlet of the common carotid artery is 300. The dotted line outlines the vessel wall.

flow are apparent near the wall both in the internal and external carotid arteries. In CE conditions, positive values of $\tilde{\varphi_f}$ are observed when the velocity component transverse to the main flow direction is from left to right (internal carotid artery), whereas negative values are observed

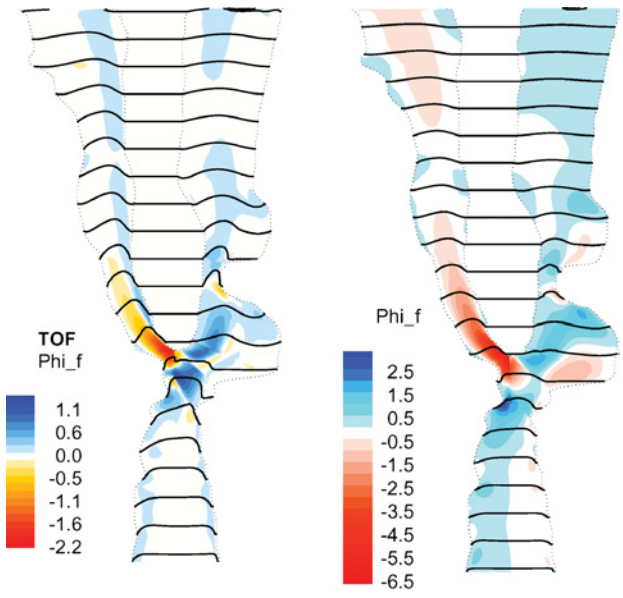

FIGURE 9. Isovalues of the phase $\tilde{\varphi_f}$ (color map) and of the image plane coordinate $\hat{y}$ (continuous lines) obtained with TOF parameters (*left*) and CE parameters (*right*). Frequency encoding is transverse to the main flow direction. Reynolds number at the inlet of the common carotid artery is 300. The dotted line outlines the vessel wall.

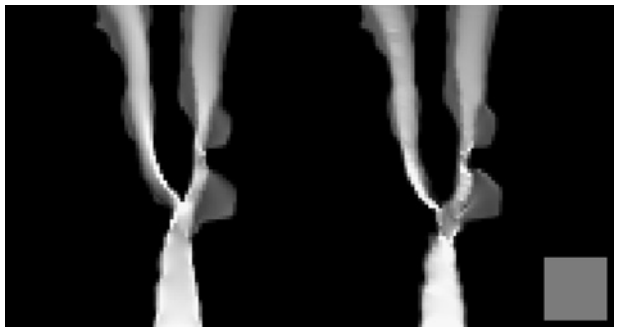

FIGURE 10. Simulated TOF-MRAs. Phase encoding is transverse to the main flow direction (*left*) or aligned with the main flow direction (*right*). The square at the right bottom shows the grey level obtained for the surrounding tissue ($T_1 = 500$ ms) using Eq. (31). Reynolds number at the inlet of the common carotid artery is 300.

when the transverse velocity component is from right to left (external carotid artery). Thus, strong phase gradients are noted at the flow divider. In TOF conditions, due to velocity compensation, $\tilde{\varphi_f}$ is significant in areas of transverse acceleration.

Simulated MRAs

In the following, the field of view of the simulated MRAs is 50 mm $\times$ 50 mm. A 100 $\times$ 100 matrix is used, giving in-plane resolution of 0.5 mm $\times$ 0.5 mm.

Figure 10 (left) displays the TOF-MRA simulated when phase encoding is transverse to the main flow direction. The overall MRA appearance is determined by saturation of the longitudinal magnetization (see Fig. 5, left), misregistration and phase dispersion (see Fig. 8, left). In particular, due to saturation, image intensity is very low in the recirculation areas. Due to IVPD, it is markedly reduced at the end of the common carotid artery and slightly reduced at the stenosis throat. On the contrary, due to misregistration, a strong signal enhancement is observable at the bifurcation apex and behind the divider wall of the external carotid artery (i.e. outside the true flow lumen). As a result, the apparent angle between the dividers walls is more acute than in the physical plane.

Figure 10 (right) displays the TOF-MRA obtained when frequency encoding is perpendicular to the main flow direction. In that case (see Fig. 9, right), misregistration and phase dispersion concurrently lead to signal dropout at the apex of the bifurcation, at the beginning of the internal carotid artery and at the stenosis throat. Misregistration alone leads to signal enhancement along the nondivider wall of the external carotid artery and before and after the stenosis throat.

Figure 11 displays the CE-MRAs simulated when phase encoding (left) or frequency encoding (right) is perpendicular to the main flow direction. Compared to

FIGURE 11. Simulated CE-MRAs. Phase encoding is transverse to the main flow direction (*left*) or aligned with the main flow direction (*right*). The square at the right bottom shows the grey level obtained for the surrounding tissue ($T_1 = 500$ ms) using Eq. (31). Reynolds number at the inlet of the common carotid artery is 300.

TOF simulations, the contrast between blood and surrounding tissue (whose intensity, assuming $T1_{\text{Tissue}} = 500\,\text{ms}$ is displayed on the square at the right bottom of the figures) is enhanced. As expected, intensity modulation due to misregistration is smaller than in TOF simulations and areas of signal drop correlate well with areas of strong phase gradients in Figs. 8, right and 9, right. In particular, the strong phase gradients along the walls at stenosis throat when phase encoding is transverse to the main flow direction leads to a reduction of apparent throat width, even if the residual lumen is larger than the voxel resolution. This reduction of apparent throat width is shown in Fig. 12. Corresponding numerical values are given in Table 3.

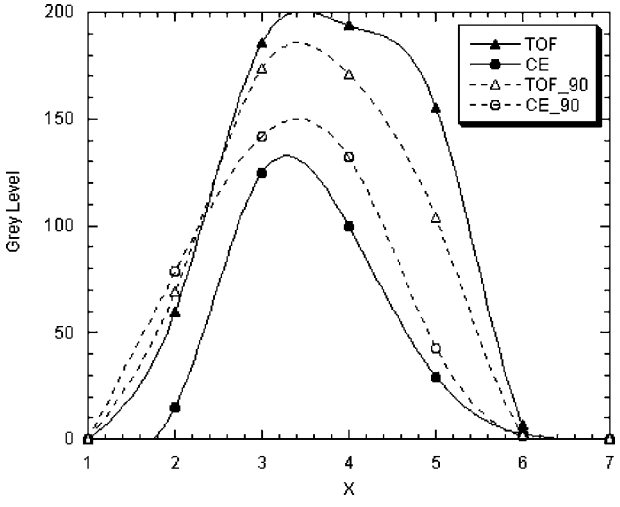

FIGURE 12. Mean image intensity in seven pixels transverse to the stenosis throat. Mean is performed over five pixels along the throat. Phase encoding is transverse to the main flow direction (TOF and CE) or aligned with the main flow direction (TOF_90 and CE_90). Reynolds number at the inlet of the common carotid artery is 300.

Comparison with Flow Phantoms Experiments

As the geometry considered for MRA simulation is two-dimensional whereas the flow phantom is three-dimensional, the following comparison is only qualitative. In addition, even if the experimental mean velocity at the inlet of the common carotid artery (0.14 ms^{-1}) closely matches the value used in the simulations (0.15 ms^{-1} when the inlet Reynolds number is 300), the experimental Reynolds number is approximately 900 due to the lower viscosity of water compared to blood. Consequently, the experimental flow structure does not exactly correspond to the simulated one (see Fig. 4 of ref. 23): the main difference is the spatial extent of the elongated recirculation area downstream of the stenosis. However, experimental and numerical values of the spin transit time are identical. Thus, the orders of magnitude of misregistration and IVPD should be similar.

Figure 13 (left) shows the TOF-MRA of the flow phantom in a coronal plane nearly corresponding to the plane used in the calculations, with frequency-encoding transverse to the main flow direction. Areas of maximal intensity are highlighted (dotted region) in the right part of the same figure. Signal dropout is observable at the apex of the bifurcation, at the beginning of the internal carotid artery and at the stenosis throat, whereas signal enhancement can be seen along the nondivider wall of the external carotid artery and before the stenosis throat, which compares well with

TABLE 3. Stenosis throat width (in pixels).

	TOF	CE	TOF 90	CE 90
$Re = 300$	3.1	2.0	3.0	2.8
$Re = 600$	3.5	1.9	3.0	2.8

Note. The stenosis throat width is defined by the width at median height of the mean image intensity in seven pixels transverse to the stenosis throat (see Fig. 12). One pixel is 0.5 mm $\times$ 0.5 mm. Throat width in the physical plane is 1.4 mm.

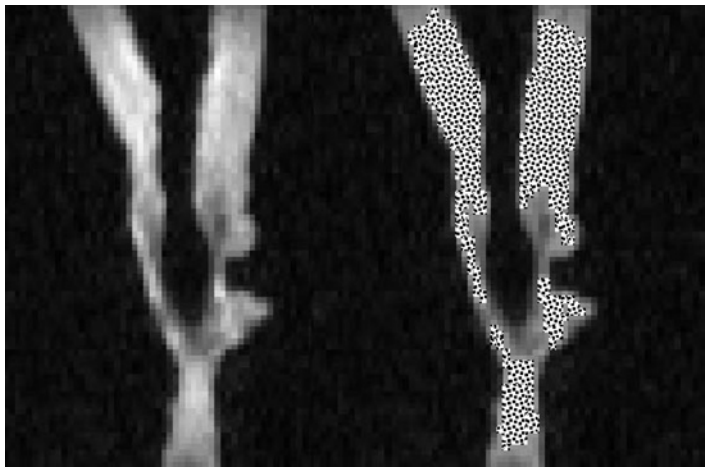

FIGURE 13. Flow-phantom experimental TOF-MRA (*left*) with high intensity areas highlighted by the dotted area (*right*). Frequency encoding is perpendicular to the main flow direction.

the corresponding simulated MRA (Fig. 10, right). An additional area of signal dropout is apparent just downstream of the stenosis throat, which might be due to flow instabilities probably arising in the jet area at the high experimental Reynolds number.

Figure 14 (left) shows the CE-MRA of the flow phantom with phase-encoding transverse to the main flow direction. Areas of signal dropout, indicated by arrows on the figure, compare well with areas of signal dropout in the corresponding simulated MRA (Fig. 11, left), highlighted by thresholding in Fig. 14 (right). Both their localization and spatial extent are similar.

In addition, the reduction of apparent stenosis throat width obtained in CE conditions when phase-encoding is perpendicular to the flow direction (see Table 3) has already been reported, both clinically and in the same flow phantom as we have used.[26]

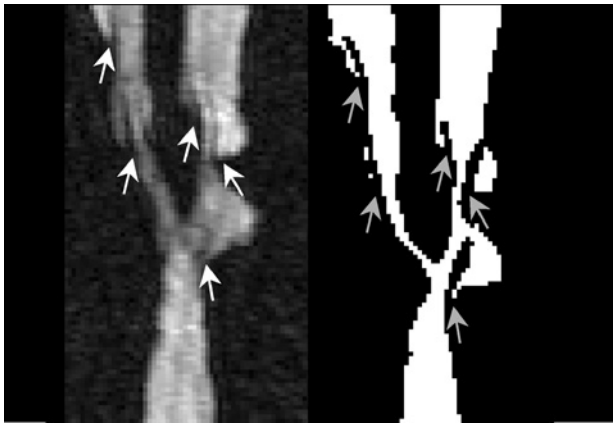

FIGURE 14. Flow-phantom experimental CE-MRA (*left*) and simulated CE-MRA after thresholding (*right*). Phase encoding is transverse to the main flow direction. Arrows indicate areas of signal loss.

Finally, even if the simulated intensity is significantly underestimated in bidimensional recirculation areas, simulated MRAs are in qualitative agreement with MR phantom experiments performed in comparable conditions, for both TOF and CE sequences and whatever the phase and frequency-encoding directions.

CONCLUSION

Numerical simulations of MRAs in a severely stenotic carotid artery bifurcation with realistic shape have been presented and validated by qualitative comparisons with MR phantom experiments. To the best of our knowledge, these simulations, even if bidimensional and steady, are the first numerical simulations of MRAs in a complex anatomically realistic geometry.

The numerical method for performing such simulations is based on the Eulerian approach proposed by Jou and Saloner[9] with further improvements of the phase-averaging procedure, which have been suggested by the signal processing perspective adopted in the current work. In particular, the approximate calculation of the jacobian of the transformation between physical and image plane meshes is avoided, as well as the determination of all the computational mesh quadrangles that map to every voxel of the image plane. Instead, both phase averaging and misregistration effects are determined by a simple geometric procedure for calculating polygon intersections. This important simplification could be helpful to extend the present work to complex three-dimensional geometries: first, the simple geometric procedure used in the present work can be applied in spaces of any dimension to determine the intersection area of general polyhedra[4]; second, this procedure can be easily used with unstructured meshes, often used in complex three-dimensional flow computations.[3] In particular, the simulation of a 2D-TOF-MRA sequence in

a three-dimensional geometry might be done by slightly modifying the proposed method. To this end, the three-dimensional velocity field has first to be computed using a 3D-CFD approach. Then, the transport of magnetization has to be calculated in three dimensions with the following modified condition for the excitation range: Eq. (4) is still holding for spins contained in the slice-selected plane and $M_z^+ = M_z^-$, $M_t^+ = M_t^-$ and $\varphi^+ = \varphi^-$ holds elsewhere. The procedure for image construction has then to be adapted in order to account for misregistration in the $\boldsymbol{k}$ direction, transformation $\mathcal{T}$ matching the slice-selected plane to a general surface in three dimensions. This would allow a quantitative comparison of simulations and experiments, required before further clinical application.

However, the methodology presented here is not valid for unsteady flows if the time scale of velocity variations is of same order, or shorter, than the time scale of the MR sequence. Thus, even under steady inflow conditions, this methodology is not valid at high Reynolds number when chaotic instabilities are present, which appear for smaller Reynolds number in three-dimensional experimental flows[1] than in bidimensional computations.[23] On the contrary, if the time scale of the velocity variations is large compared to the time scale of the MR sequence, MRAs of unsteady flows, such as physiological pulsatile flows, can be simulated by our methodology coupled to the look-up approach previously used in an idealized model of the carotid bifurcation.[9]

ACKNOWLEDGMENTS

We would like to thank Francis Cassot (INSERM U455, Toulouse, France) for stimulating discussions and interesting comments, Vitaliy Rayz (UC Berkeley) for help with CFDRC software, as well as Hervé Neau (IMFT) for technical support and Paul Duru for his extremely careful reading of the manuscript. Sylvie Lorthois was the recipient of a postdoctoral "Lavoisier Grant" from the French "Ministère des Affaires Etrangères." In addition, this work has been supported by the "France-Berkeley Fund."

APPENDIX A: CHARACTERISTIC TIMES FOR PRECESSION

The orders of magnitudes of the characteristic times for precession in Eqs. 10 and 11 are $2\pi/(U_0\gamma\tau\mathcal{G}_f)$ and $2\pi/(U_0\gamma T_p\mathcal{G}_p)$, respectively. As the frequency-encoding and phase-encoding gradients intensities are chosen in order to scan a field of view corresponding to the domain of interest, *i.e* of order L, we have:

$$\gamma\tau\mathcal{G}_f \sim \gamma T_p\mathcal{G}_p \sim \frac{2\pi}{L} \tag{A.1}$$

Thus, the characteristic times for precession are the same in Eqs. 10 and 11 and equal the characteristic spin transit time L/U_0.

APPENDIX B: SIGNAL INTENSITY IN A VOXEL: ONE-DIMENSIONAL DEMONSTRATION

Let first rewrite Eq. (22) at constant x and thus constant X:

$$I(Y) = \frac{1}{(2\pi)^2}\int_y \mathcal{M}(y)\delta\left(y+\tilde{y}(y)-Y\right)dy. \tag{B.1}$$

The corresponding transformation $\mathcal{T}$ of space ($\hat{y} = y + \tilde{y}(y)$) is not a bijection. Let us consider the particular case sketched in Fig. 15, where Y has two antecedents y_a and y_b. In that case, Eq. (B.1) leads to

$$I(Y) = \frac{1}{(2\pi)^2}\left(\int_{E^-}\mathcal{M}(y)\delta\left(y+\tilde{y}(y)-Y\right)dy + \int_{E^+}\mathcal{M}(y)\delta\left(y+\tilde{y}(y)-Y\right)dy\right), \tag{B.2}$$

$\mathcal{T}$ being a bijection on each separate domain E^- and E^+ of the physical plane with inverse transformations respectively being $\mathcal{T}_-^{-1}$ and $\mathcal{T}_+^{-1}$. Thus,

$$I(Y) = \frac{1}{(2\pi)^2}\left(\int_{\mathcal{T}(E^-)}\mathcal{M}\circ\mathcal{T}_-^{-1}(\hat{y})\delta\left(\hat{y}-Y\right)\frac{d\mathcal{T}_-^{-1}}{d\hat{y}}(\hat{y})\,d\hat{y} + \int_{\mathcal{T}(E^+)}\mathcal{M}\circ\mathcal{T}_+^{-1}(\hat{y})\delta\left(\hat{y}-Y\right)\frac{d\mathcal{T}_+^{-1}}{d\hat{y}}(\hat{y})\,d\hat{y}\right), \tag{B.3}$$

or, defining respectively $\mathcal{M}_{-/+}(y) = \mathcal{M}(y)$ for y in $E^{-/+}$ and $\mathcal{M}_{-/+}(y) = 0$ everywhere else:

$$I(Y) = \frac{1}{(2\pi)^2}\left(\int_{\hat{y}}\mathcal{M}_-\circ\mathcal{T}_-^{-1}(\hat{y})\delta\left(\hat{y}-Y\right)\frac{d\mathcal{T}_-^{-1}}{d\hat{y}}(\hat{y})\,d\hat{y} + \int_{\hat{y}}\mathcal{M}_+\circ\mathcal{T}_+^{-1}(\hat{y})\delta\left(\hat{y}-Y\right)\frac{d\mathcal{T}_+^{-1}}{d\hat{y}}(\hat{y})\,d\hat{y}\right). \tag{B.4}$$

Finally:

$$I(Y) = \frac{1}{(2\pi)^2}\left(\mathcal{M}_-\circ\mathcal{T}_-^{-1}(Y)\frac{d\mathcal{T}_-^{-1}}{d\hat{y}}(Y) + \mathcal{M}_+\circ\mathcal{T}_+^{-1}(Y)\frac{d\mathcal{T}_+^{-1}}{d\hat{y}}(Y)\right). \tag{B.5}$$

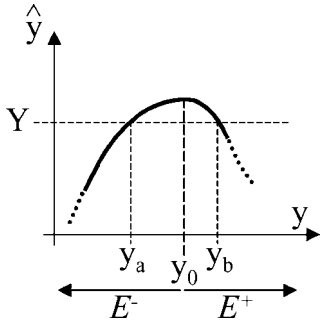

FIGURE 15. Transformation $\hat{y}(y)$ of the physical plane into the image plane, with notations used in Appendix B.

The signal intensity $\mathcal{I}$ in a voxel V is the sum of $I(Y)$ over the whole voxel:

$$\mathcal{I}(V) = \frac{1}{(2\pi)^2}\left(\int_V \mathcal{M}_- \circ \mathcal{T}_-^{-1}(Y) \frac{d\mathcal{T}_-^{-1}}{d\hat{y}}(Y)\, dY + \int_V \mathcal{M}_+ \circ \mathcal{T}_+^{-1}(Y) \frac{d\mathcal{T}_+^{-1}}{d\hat{y}}(Y)\, dY \right), \quad \text{(B.6)}$$

which simplifies to:

$$\mathcal{I}(V) = \frac{1}{(2\pi)^2}\left(\int_{\mathcal{T}_-^{-1}(V)} \mathcal{M}(y)\, dy + \int_{\mathcal{T}_+^{-1}(V)} \mathcal{M}(y)\, dy \right) = \frac{1}{(2\pi)^2} \int_{\mathcal{V}} \mathcal{M}(y)\, dy, \quad \text{(B.7)}$$

where $\mathcal{V}$ is the antecedent of V by $\mathcal{T}$ (*i.e.* $\mathcal{T}(\mathcal{V}) = V$). Note that the same argument is valid for a higher number of antecedents or for cases where the number of antecedents is not uniform throughout the voxel.

APPENDIX C: AREA OF POLYGONS AND POLYGON INTERSECTIONS

By construction of the CFD grid, $\mathcal{E}$ is a simple quadrangle[5] whose area is given by

$$\mathcal{A}(\mathcal{E}) = \frac{1}{2} \sum_{i=1}^{N} (x_i y_{i\oplus 1} - x_{i\oplus 1} y_i), \quad \text{(C.1)}$$

where (x_i, y_i) are the coordinates of the ith edge of $\mathcal{E}$, $N = 4$, and $(N \oplus 1 = 1)$.

However, due to misregistration, $\mathcal{T}(\mathcal{E})$ is not necessarily a simple quadrangle but may be self-intersecting. In this case, the intersection point is considered as two superimposed additional vertices. In other words, the self-intersecting quadrangle is considered as a six vertices simple polygon, whose area is calculated by Eq. (C.1) with $N = 6$.

The procedure for calculating polygon intersections has been described elsewhere[15,16]: briefly, the intersection points of both polygons are calculated and used to generate a new decomposition in simplices of both polygons, considering the new edges obtained from the intersection points. Once the new decomposition is established, a triangle-based description for polygons[16] is used, where they are represented as layers of original triangles (i.e., triangles including two consecutive edges of the polygon and the origin of coordinates). The level of each original triangle according to an order relationship, the so-called subordination relationship, is subsequently determined. By definition of this relationship, an original triangle $t = OP_1P_2$ is subordinated to an original triangle $s = OQ_1Q_2$ if and only if $t = s$ or, in the case that $t \neq s$, it exists a point belonging to the interior of the segment P_1P_2 that also belongs to the interior of s. In addition, the relationship of subordination of each original triangle S_i of the first polygon with respect to each original triangle U_j of the second polygon is studied. Finally, several triangles from both polygons are selected according to criterions described in ref. 15. In particular, if S_i is not subordinated to any U_j, it does not belong to the intersection. If S_i is subordinated to one and only one U_j of a given level, it belongs to the intersection. The intersection area is obtained by summing the areas of all the original triangles belonging to the intersection. Note that this procedure is robust and efficient, and that no additional study of particular cases is needed.

REFERENCES

[1] Bale-Glickman, J., K. Selby, D. Saloner, and O. Savas. Experimental flow studies in exact-replica phantoms of atherosclerotic carotid bifurcations under steady input conditions. *ASME J. Biomech. Eng.* 125:38–48, 2003.

[2] Botnar, R., G. Rappitsch, M. B. Scheideggerr, D. Liepsch, K. Perktold, and P. Boesiger. Hemodynamics in the carotid artery bifurcation: A comparison between numerical simulations and in vitro MRI measurements. *J. Biomech.* 20:137–144, 2000.

[3] Butty, V. D., K. Gudjonsson, P. Buchel, V. B. Makhijani, Y. Ventikos, and D. Poulikakos. Residence times and basins of attraction for a realistic right internal carotid artery with two aneurysms. *Biorheology* 39:387–393, 2002.

[4] Feito, F. R., and M. Rivero. Geometric modeling based on simplicial chains. *Comput. Graphics* 22:611–619, 1998.

[5] Feito, F. R., J. C. Torres, and A. Urena. Orientation, simplicity, and inclusion test for planar polygons. *Comput. Graphics* 19:596–600, 1995.

[6] Gao, J., and J. C. Gore. A numerical investigation of the dependance of NMR signal from pulsatile blood flow in CINE pulse sequences. *Med. Phys.* 18:342–349, 1991.

[7] Gatenby, J. C., T. R. McCauley, and J. C. Gore. Mechanisms of signal loss in magnetic resonance imaging of stenoses. *Med. Phys.* 20:1049–1057, 1993.

[8] Jou, L. D., R. Van Tyen, S. A. Berger, and D. Saloner. Calculation of the magnetization distribution for fluid flow in curved vessels. *Magn. Res. Med.* 35:577–584, 1996.

[9] Jou, L. D., and D. Saloner. A numerical study of magnetic resonance images of pulsatile flow in a two dimensional carotid bifurcation. *Med. Eng. Phys.* 20:643–652, 1998.

[10] Liang, Z., and P. C. Lauterbur. Principles of Magnetic Resonance Imaging: A signal processing perspective. IEEE Press Series on Biomechanical Engineering, New York, 2000.

[11] Ladak, H. M., J. S. Milner, and D. A. Steinman. Rapid three-dimensional segmentation of the carotid bifurcation from serial MR images. *ASME J. Biomech. Eng.* 122:96–99, 2000.

[12] Perktold, K., M. Hofer, G. Rappitsch, M. Loew, B. D. Kuban, and M. H. Friedman. Validated computation of physiologic flow in a realistic coronary artery branch. *J. Biomech.* 31:217–228, 1998.

[13] Rapp, J. H., and D. Saloner. Current status of carotid imaging by MRA. *Cardiovasc. Surgery* 11:445–447, 2003.

[14] Redaelli, A., G. Rizzo, S. Arrigoni, E. Di Martino, D. Origgi, F. Fazio, and F. Montevecchi. An assisted automated procedure for vessel geometry reconstruction and hemodynamic simulations from clinical imaging. *Comput. Med. Imaging Graph.* 26:143–152, 2002.

[15] Rivero, M., and F. R. Feito. Boolean operations on general planar polygons. *Comput. Graph.* 24:881-896, 2000.

[16]Rueda, A. J., F. R. Feito, and M. Rivero. A triangle-based representation for polygons and its applications. *Comput. Graph.* 26:805–814, 2002.

[17]Saloner, D., R. Van Tyen, W. P. Dillon, L. D. Jou, and S. A. Berger. Central intraluminal saturation stripe on MR angiograms of curved vessels: Simulation, phantom and clinical analysis. *Radiology* 198:733–739, 1996.

[18]Schwartz. J. Méthodes mathématiques pour les sciences physiques. Collection Enseignement des Sciences, Hermann, Paris, 1998.

[19]Siegel, J. M., J. N. Oshinski, R. I. Pettigrew, and D. N. Ku. Comparison of phantom and computer-simulated MR images of flow in a convergent geometry: Implications for improved two-dimensional MR angiography. *J. Magn. Res. Imaging* 5:677–683, 1995.

[20]Siegel, J. M., J. N. Oshinski, R. I. Pettigrew, and D. N. Ku. Computational simulation of turbulent signal loss in 2D time-of-flight magnetic resonance angiograms. *Magn. Res. Med.* 37:609–614, 1997.

[21]Steinman, D. A., C. R. Ethier, and B. K. Rutt. Combined analysis of spatial and velocity displacement artifacts in phase contrast measurements of complex flows. *J. Magn. Res. Imaging* 7:339–346, 1997.

[22]Stroud, J. S., S. A. Berger, and D. Saloner. Influence of stenosis morphology on flow through severely stenotic vessels: Implications for plaque rupture. *J. Biomech.* 33:443–455, 2000.

[23]Stroud, J. S., S. A. Berger, and D. Saloner. Numerical analysis of flow through a severely stenotic carotid artery bifurcation. *ASME J. Biomech. Eng.* 124:9–20, 2002.

[24]Svensson, J., J. S. Petersson, F. Stahlberg, E. M. Larsson, P. Leander, and L. E. Olsson. Image artifacts due to a time-varying contrast medium concentration in 3D contrast-enhanced MRA. *J. Magn. Reson. Imaging* 10:919–28, 1999.

[25]Tambasco, M., and D. A. Steinman. On assessing the quality of particle tracking through computational fluid dynamics models. *ASME J. Biomech. Eng.* 124:166–175, 2002.

[26]Townsend, T. C., D. Saloner, X. M. Pan, and J. H. Rapp. Contrast material-enhanced MRA overestimates severity of carotid stenosis, compared with 3D time-of-flight MRA. *J. Vasc. Surg.* 38:36–40, 2003.

[27]Van Tyen, R., D. Saloner, L. D. Jou, and S. A. Berger. MR imaging of flow through tortuous vessels: A numerical simulation. *Magn. Res. Med.* 31:184–195, 1994.

[28]Vlaardingerbroek, M. T., and J. A. Boer. Magnetic Resonance Imaging: Theory and Practice. Berlin: Springer Verlag, 1996.